RSC Advances

PAPER

View Article Online
View Journal | View Issue

Cite this: *RSC Adv.*, 2021, **11**, 6842

Synergistic effect of cocatalytic $NiSe_2$ on stable 1T-MoS_2 for hydrogen evolution†

Zhen Li,[a] Xinzhi Ma,[a] Lili Wu, *[ab] Hongfeng Ye,[a] Lu Li,[a] Shuangyan Lin,[c] Xitian Zhang,[a] Zhitao Shao,[a] Yue Yang[a] and Hong Gao *[a]

Received 20th January 2021
Accepted 2nd February 2021

DOI: 10.1039/d1ra00506e

rsc.li/rsc-advances

Robust and economical catalysts are imperative to realize the versatile applications of hydrogen. Herein, a 1T-MoS_2/N-doped $NiSe_2$ composite was rationally synthesized *via* a solvothermal method, in which the MoS_2 nanosheets have a stable 1T phase structure, and the $NiSe_2$ nanoparticles serve as a cocatalytic support for MoS_2. The nonnegligible electronic couplings between $NiSe_2$ and MoS_2 could facilitate the optimization of their electronic structure and then improve the hydrogen adsorption. What is more, the nitrogen dopants in the $NiSe_2$ nanoparticles could intensify the intercalation of ammonium ions in the 1T-MoS_2 nanosheets, and further enlarge their interlayer spacing, thus the electrolyte could infiltrate into the catalyst more easily and sufficiently. This work provides a new route for rationally designing highly active and low cost hydrogen evolution reaction (HER) catalysts, and enriches the study of transition metal chalcogenides toward HER.

1. Introduction

Hydrogen is recognized as a promising clean energy resource because of its high gravimetric energy density and no CO_2 release.[1–4] Among the existing H_2 production methods, electrochemical and photocatalytic hydrogen evolution by water splitting have been widely recognized as the most promising strategies.[5–7] Especially, electrochemical technology has significant advantages due to its quick, straightforward and highly efficient fashion.[8–10] Generally, to achieve a fast H_2 production rate, a catalyst with high efficiency is necessary. Up to now, platinum (Pt)-based catalysts have been widely considered as the best catalysts for HER. However, their limitations such as being expensive and having frustrating durability severely restricted their scale-up commercial applications.[11–13] Thus, the rational design and fabrication of economic and durable HER catalysts are of great importance.

Transition metal dichalcogenides (TMDs) have attracted considerable attention in substituting Pt-based catalysts due to their excellent electrocatalytic properties, popular price, and abundant earth reserves.[14] Molybdenum disulfide (MoS_2) is one of the most representative TMDs. Notably, the typical lamellar characterizations and structural polymorphism grant it distinctive characteristics in the electrochemical field.[15] Generally, MoS_2 is in a 2H phase, which is thermodynamically stable. 2H-MoS_2 is semiconductor and has a poor conductivity. Besides, the large inert basal planes and small proportion of active edges significantly limits its catalytic efficiency.[16,17] In comparison with 2H-MoS_2, the metallic (1T) phase MoS_2 has a good conductivity and possesses excellent HER response both on basal plane and at edge sites. However, the microstructure of 1T-MoS_2 is thermally metastable and would gradually convert into 2H-phase even at room temperature.[17] Thus, stable 1T-MoS_2 catalysts are highly pursued for the applications in hydrogen evolution. Typically, Wu *et al.* successfully prepared osmotically swollen MoS_2, in which adjacent layers are intercalated by ammonium ions with remarkable lattice expansion. The swollen MoS_2 catalyst exhibits excellent HER activity with a small Tafel slope of 45 mV dec^{-1}.[18] However, the HER performances are still unsatisfied. Constructing heterogeneous interfaces by introducing another component is an efficient way to boost the electrochemical activity of catalysts.[19–23] As is known to all, HER proceeds with the initial formation of hydrogen intermediates (H*) followed by a Tafel or Heyrovsky step. The synergistic effect between two hybridized components could fine tune their surface adsorption properties by interfacial electronic coupling and facilitate an excellent activity and a high stability towards HER. For example, Song *et al.* bounded 1T-MoS_2 nanopatches to highly conductive single-walled carbon nanotube films relying on interface engineering and realized a further improved overpotential of 108 mV.[23] Regrettably, the single-walled carbon nanotube films exhibit scarce catalytic activity, and just behave as the conductive skeletons at the expense of the catalyst

[a]*Key Laboratory for Photonic and Electronic Bandgap Materials, Ministry of Education, School of Physics and Electronic Engineering, Harbin Normal University, Harbin 150025, China. E-mail: wll790107@hotmail.com; gaohong65cn@126.com*

[b]*Center for Engineering Training and Basic Experimentation, Heilongjiang University of Science and Technology, Harbin 150022, China*

[c]*School of Chemistry, Guangdong University of Petrochemical Technology, Maoming, Guangdong, 525000, PR China*

† Electronic supplementary information (ESI) available. See DOI: 10.1039/d1ra00506e

weight. Recently, the heterogeneous TMDs with a relatively high conductivity are considered to be used as a cocatalytic support for MoS_2 due to their excellent cocatalytic functionality.[24,25] Typically, Yang' group chose conductive NiS_2 to construct 1T-MoS_2/NiS_2 hybrid catalyst and realized a low onset potential of 34 mV.[26] Although extensive efforts have been devoted, the development of heterogeneous TMDs catalyst still lies in its early stage.

In this work, N-doped $NiSe_2$ nanoparticles were selected as the cocatalytic support for 1T-MoS_2 nanosheets. The non-negligible electronic couplings between $NiSe_2$ and MoS_2 could facilitate the optimization of their electronic structure and then improve their hydrogen adsorption. In addition, the nitrogen dopants in the $NiSe_2$ nanoparticles could further enlarge the (002) interlayer spacing of MoS_2, which makes electrolyte infiltrate into the catalyst more easily and sufficiently. This work enriches the study on heterogeneous TMDs catalyst for HER and provides a new option to realize stable 1T-MoS_2.

2. Experimental

2.1 Chemicals and reagents

Nickel chloride hexahydrate ($NiCl_2 \cdot 6H_2O$, 98%), sodium borohydride ($NaBH_4$, 98%), selenium (Se, 99.9%), thiourea ($CS(NH_2)_2$, 99%), ammonium molybdate ($(NH_4)_6Mo_7O_{24} \cdot 4H_2O$, 99%), disodium hydrogen phosphate dodecahydrate ($Na_2HPO_4 \cdot 7H_2O$), sodium phosphate monobasic dihydrate ($NaH_2PO_4 \cdot 2H_2O$) are all analytical grade. They were used without further purification.

2.2 Materials syntheses

Bare $NiSe_2$ nanoparticles were synthesized by solvothermal method. First, 0.316 g selenium and 0.189 g $NaBH_4$ were dissolved in 30 mL *N*,*N*-dimethylformamide (DMF) and stirred for 1 hour. Then, 0.476 g $NiCl_2 \cdot 6H_2O$ was gradually added into the solution and agitated for 1 hour. After that, the solution was poured into a Teflon-lined autoclave, whose volume is 50 mL. The autoclave was kept at 160 °C for 12 hours. Centrifugal method was adopted to gather the precipitate. Deionized water and ethanol were alternatively used as cleaning fluid. Finally, the collected precipitate was dried at 60 °C in vacuum overnight.

To synthesize MoS_2/$NiSe_2$ composite, 76 mg of as-prepared $NiSe_2$ powder was dispersed in 30 mL deionized water and sonicated for 30 min. Then 62 mg $(NH_4)_6Mo_7O_{24} \cdot 4H_2O$ and 114 mg $CS(NH_2)_2$ were added into the solution and stirred homogeneously. The dispersion was kept at 180 °C for 24 hours. The collection and treatment of the precipitate are the same as above.

The synthesis of bare MoS_2 nanosheets is the same as that for MoS_2/$NiSe_2$ composite expect for adding $NiSe_2$ nanoparticles as substrates.

2.3 Fabrication of electrodes

The prepared catalysts and carbon nanotubes were dispersed in the solvent of *N*-methyl-2-pyrrolidone (NMP) including 7 wt% PVDF (mass ratio of catalysts, PVDF, and carbon nanotubes was 8 : 1 : 1). After ultrasonic uniformity, the slurry was coated on carbon paper (mass loading: 1 mg cm^{-2}), and dried at 60 °C for 12 h under vacuum condition.

2.4 Materials characterization

The crystal structure was characterized by X-ray diffraction (XRD, D/max 2600, Rigaku, Japan) with Cu Kα radiation (λ = 1.5418 Å). The micromorphology and elementary composition were determined by scanning electron microscopy (SEM, SU70, Hitachi, Japan) equipped with energy dispersive X-ray spectroscopy (EDS) and transmission electron microscopy (TEM, FEI, Tecnai TF20). The surface chemical states were characterized by X-ray photoelectron spectroscopy (XPS) employing K-alpha X-ray spectrometer (Thermo, USA).

2.5 Electrocatalytic measurements

The VMP3 electrochemical workstation (Bio-logic, France) was used to conduct electrochemical measurements. The experiments were carried out within a typical three-electrode system in 0.5 M H_2SO_4 electrolyte (except where noted). The prepared catalysts coated on carbon paper was used as working electrode with saturated calomel electrode (SCE) and carbon rod as reference and counter electrodes, respectively. The formula E (RHE) = E (SCE) + 0.059 × pH + 0.241 V was used to convert potentials into the reversible hydrogen electrode defined as (RHE). Polarization curves were attained using a linear sweep voltammetry (LSV) method. All the polarization curves were corrected using 85% ohmic potential drop (iR) compensation. The electrochemical impedance spectroscopy (EIS) was measured at the overpotential of −0.2 V (*vs.* RHE) with the frequencies ranging from 100 mHz to 100 KHz. Electrochemical surface area (ECSA) was estimated by the cyclic voltammetry (CV) measurements at 20–100 mV s^{-1}. By plotting the different scan rate of anode and cathode current density difference ($\Delta j = j_a - j_c$) at 0.15 V (*vs.* RHE), double-layer capacitance (C_{dl}) is defined as half of the slopes value. Turnover frequency (TOF) of the catalysts was calculated by employing the CV curves measured in pH = 7 phosphate buffer. The voltage range is from −0.2 to 0.6 V (*vs.* RHE), and the scan rate is 50 mV s^{-1}. The calculation follows the equation: TOF (s^{-1}) = ($j \times A$)/($2 \times n \times F$), where F is the Faraday's constant (96 485 C mol^{-1}), j (mA cm^{-2}) is the current density obtained by LSV measurement, A (cm^2) is the geometric area of the electrodes, and the number of 2 represents that two electrons are required to form one hydrogen molecule from two protons ($2H^+ + 2e^- = H_2$). Catalytic stability was examined by the CV test at 50 mV s^{-1} from −0.3 to 0.1 V (*vs.* RHE) and the chronoamperometry measurement at −100 mV (*vs.* RHE) for 25 h.

3. Results and discussion

3.1 Morphologies and structures

Fig. 1a illustrates the preparation process of MoS_2/$NiSe_2$ composite. Firstly, $NiSe_2$ nanoparticles were prepared *via* a solvothermal method. The SEM image in Fig. S1† well exhibits their irregular polyhedral morphology with a large amount of ridges and re-entrants. EDS analysis reveals that the as-prepared nanoparticles are slightly nonstoichiometric $NiSe_2$ with a small amount of nitrogen dopant (Fig. S2†). Secondly, the N-doped $NiSe_2$ nanoparticles were dispersed into a homogeneous aqueous solution of ammonium molybdate and thiourea to *in*

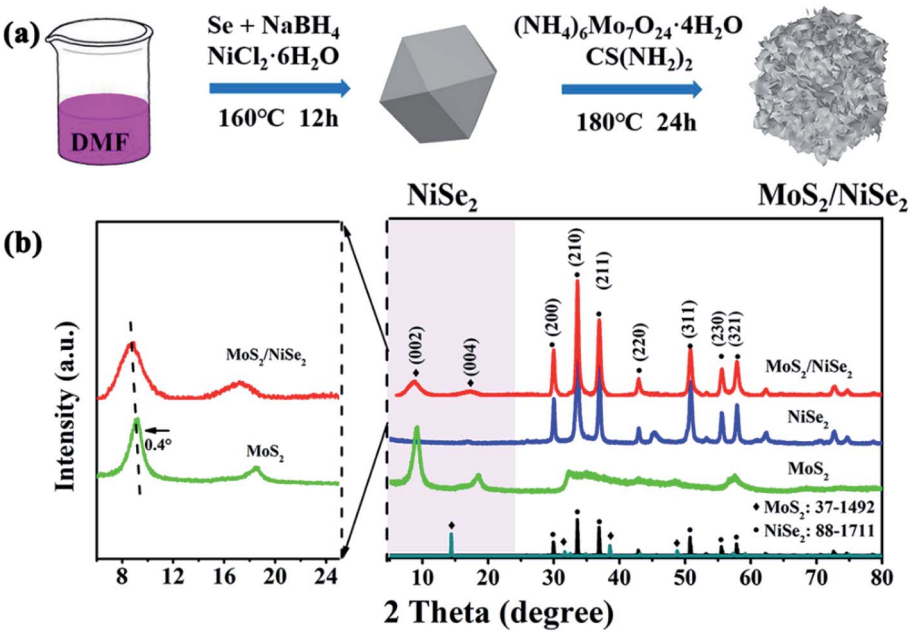

Fig. 1 (a) Diagrammatic drawing of the synthesis process of $MoS_2/NiSe_2$ composite, in which DMF stands for *N*,*N*-dimethylformamide. (b) XRD patterns of bare MoS_2, $NiSe_2$, and $MoS_2/NiSe_2$ composite.

situ grow MoS_2 nanosheets on their surface. The resultant compositions were firstly characterized by XRD. In Fig. 1b, the XRD profile consists of dominant sharp diffraction peaks of cubic $NiSe_2$ (JCPDS 88-1711) and faint signals of MoS_2. Notably, the (002) peak of MoS_2 is located at 8.7°, which shows a remarkable negative shift from the (002) peak of 2H-phase MoS_2 (JCPDS 37-1492), demonstrating that the MoS_2 nanosheets have a 1T-phase structure and the resultant products are 1T-MoS_2/N-doped $NiSe_2$ composite. The bare MoS_2 nanosheets prepared without N-doped $NiSe_2$ nanoparticles participating also have a 1T-phase structure with their (002) peak located at 9.1°. It powerfully indicates that the MoS_2 synthesized in this study, either bare or in composite, are both in 1T phase. More importantly, the 1T-MoS_2 is thermodynamically stable, which is proved by almost the same XRD pattern obtained from the sample aged 3 months at room temperature (Fig. S3†).

The morphology of the 1T-MoS_2/N-doped $NiSe_2$ composite was vividly shown in Fig. 2a. It is clear that a sight of flimsier nanosheets intertwine into an edge-oriented geometry on the outer surface of N-doped $NiSe_2$ nanoparticles. The nanosheets distribute more homogeneously than those ones prepared without N-doped $NiSe_2$ nanoparticles participating (Fig. S4†). It should give the credit of this homogeneous distribution to the abundant and highly dispersed nucleation sites provided by the N-doped $NiSe_2$ nanoparticles. EDS analysis reveals that S, Mo, Se and Ni elements coexist in the composite with a small amount (~6.7 at%) of N element (inset of Fig. 2a), which should be inherited from DMF, thiourea and ammonium molybdate. The elemental mappings in Fig. 2b demonstrate the uniformly dispersion of Ni, Se, Mo, S, and N. The luminosities of Ni, Se, Mo and S elements are markedly higher than that of N element, illustrating the relatively low content of N element. The distributions of Mo and S have a slightly larger size than those of Ni and Se, corresponding to the decoration of $NiSe_2$ nanoparticles with the MoS_2 nanosheets. The further microstructural information of the 1T-MoS_2/N-doped $NiSe_2$ composite was characterized by TEM. Fig. 2c shows that the composite consists of internal $NiSe_2$ nanoparticle (dark area) and external translucent MoS_2 nanosheets. The ultrathin MoS_2 nanosheets are less than five layers and tightly wrap the $NiSe_2$ nanoparticle, which generates abundant interfaces between MoS_2 and $NiSe_2$. The typical high-resolution TEM image offers a deep insight to these heterogeneous interfaces (Fig. 2d). The lattice distance of 0.27 nm is assigned to the (210) plane of $NiSe_2$, and the one of 1.02 nm is the (002) plane of 1T-MoS_2.[27,28] Impressively, the (002) lattice distance of 1.02 nm for 1T-MoS_2 is 0.4 nm larger than 2H-MoS_2 (~0.62 nm), and coincides with the diffraction peak located at 8.7° in the XRD curve (Fig. 1b). This increment just well accommodate ammonium ions, whose size is about 0.35 nm.[29,30] Thus, the enlarged (002) interlayer spacing of MoS_2 in this study should owe to the intercalation of ammonium ions inherited from thiourea or ammonium molybdate. Fig. S5† is the high-resolution TEM image of bare MoS_2 nanosheets. It is noticeable that the (002) interlayer spacing of the MoS_2 in composite is further enlarged with a ~5% expansion by hybridizing with N-doped $NiSe_2$ nanoparticles. Fig. 2e shows the SAED pattern of the 1T-MoS_2/N-doped $NiSe_2$ composite, wherein the (110) and (105) planes belong to 1T-MoS_2, and the (200), (210), (211) and (220) planes belong to N-doped $NiSe_2$. The discrete concentric rings well demonstrate the polycrystalline nature of the 1T-MoS_2/N-doped $NiSe_2$ composite.

The compositions and chemical surface states of 1T-MoS_2/N-doped $NiSe_2$ composite were analyzed by XPS. Fig. 3a indicates the existence of Ni, Se, Mo, S, and N. Fig. 3b shows the Mo-3d spectra, in which Mo^{4+}, Mo^{5+}, and Mo^{6+} were included. The peak located at 235.7 eV is corresponding to Mo^{6+}, which is

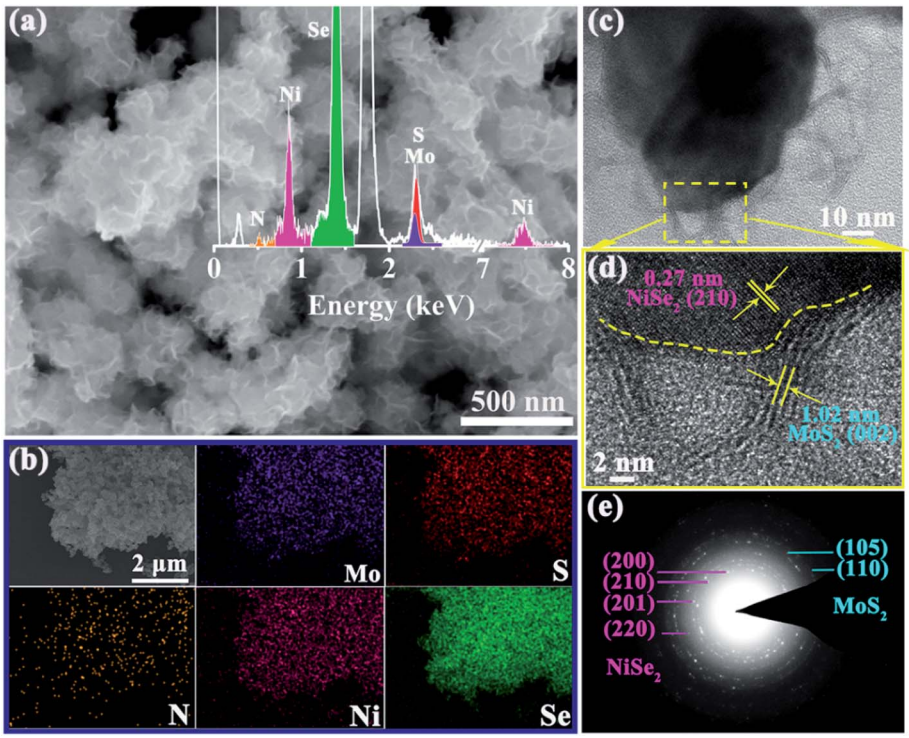

Fig. 2 (a) SEM image, inset shows the relevant EDS spectrum, (b) the corresponding elemental mapping images, (c) TEM image, (d) HRTEM image, and (e) SAED pattern of $MoS_2/NiSe_2$ composite.

derived from surface oxidation and coincided with the detected O element in Fig. 3a. The two doublets located at 232.5/229.5 eV and 231.6/228.5 eV coincide with the $3d_{3/2}$ and $3d_{5/2}$ orbits of Mo^{4+} and Mo^{5+}, respectively.[31] In the S-2p spectra (Fig. 3c), the 161.2 eV and 162.5 eV peaks belong to the S^{2-} $2p_{3/2}$ and S^{2-} $2p_{1/2}$ orbits, respectively.[32,33] Compared with bare 1T-MoS_2, these peaks all exhibit a red shift in the 1T-MoS_2/N-doped $NiSe_2$ composite. Fig. 3d shows the Ni-2p profiles, in which the peaks were divided into three doublet peaks corresponding to Ni^{2+}, Ni^{3+} and shakeup satellite. The doublets located at 853.6/871.0 eV and 856.4/874.2 eV are corresponded well with the $2p_{3/2}$ and $2p_{1/2}$ of Ni^{2+} and Ni^{3+}, and another doublets belong to the shakeup satellite of Ni 2p.[27,34] In contrast with the red shifts of Mo-3d and S-2p, the three doublets of Ni-2p all show a blue shift as compared with bare $NiSe_2$. Fig. 3e is the Se-3d XPS spectra. The Se_2^{2-} $3d_{5/2}$ and Se_2^{2-} $3d_{3/2}$ peaks located at 54.7 and 55.6 eV also show a slightly red shifting compared with bare $NiSe_2$.[35] These red/blue shifts imply the electron transfer between $NiSe_2$

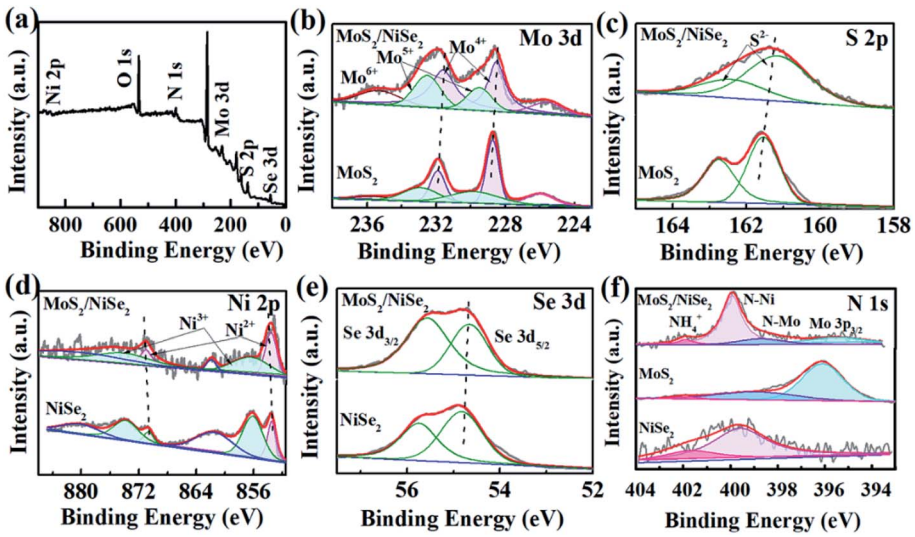

Fig. 3 (a) The survey XPS spectrum of $MoS_2/NiSe_2$, (b) Mo 3d, (c) S 2p, (d) Ni 2p, (e) Se 3d, (f) N 1s XPS spectra of $MoS_2/NiSe_2$ compared with bare MoS_2 or $NiSe_2$.

and MoS_2 at their heterogeneous interfaces and highly enhance the hydrogen adsorption ability.[23,36,37] Additionally, the ratio of Ni^{2+}/Ni^{3+} in the composite is 0.56, which significantly larger than that in the bare $NiSe_2$ (0.37). Higher Ni^{2+}/Ni^{3+} ratio always associates with a superior HER activity due to the higher sensitivity of Ni^{2+} to HER than Ni^{3+}.[38] In Fig. 3f, the N 1s XPS spectra consist of three overlapping peaks. The dominant one is located at 399.4 eV and ascribed to N–Ni bond.[39] The nanoid one at 398.2 eV belongs to N–Mo bond.[40] The significantly higher intensity of N–Ni than N–Mo bond indicates the relatively higher content of N in $NiSe_2$ than MoS_2, which might be the reason why the (002) interlayer spacing of 1T-MoS_2 is further enlarged after hybridizing with the N-doped $NiSe_2$ nanoparticles. The small peak located at 401.7 eV is corresponded to the NH_4^+ embed in the (002) interlayer of MoS_2 or located on the surface of $NiSe_2$, strongly supporting the above assertion that the expanded (002) interlayer spacing is realized by the intercalation of ammonium ions.

3.2 Electrochemical performances

The polarization curve of 1T-MoS_2/N-doped $NiSe_2$ composite is shown in Fig. 4a. When current density arrives at 10 mA cm^{-2}, the overpotential is only 94 mV, dramatically surpassing bare MoS_2 (210 mV) and $NiSe_2$ (147 mV). In Fig. 4b, the 1T-MoS_2/N doped $NiSe_2$ composite, bare MoS_2 nanosheets, and $NiSe_2$ nanoparticles exhibit a Tafel slope of 58, 76 and 63 mV dec^{-1}, respectively. They are all larger than 40 mV dec^{-1}, implying a Volmer–Heyrovsky mechanism and the rate-determining step of desorption process. Meanwhile, the lower value of 1T-MoS_2/N-doped $NiSe_2$ composite indicates its faster HER kinetics than bare MoS_2 and $NiSe_2$.[25] More than that, the excellent HER activity and low Tafel slope of 1T-MoS_2/N-doped $NiSe_2$ composite also have obvious advantages to most recently reported low-cost HER catalysts (Table S1†). From Tafel data, the exchange current density (j_0) of 240.5 μA cm^{-2} is obtained for 1T-MoS_2/N-doped $NiSe_2$ composite. It is significantly larger than that of bare $NiSe_2$ (177.6 μA cm^{-2}) and 1T-MoS_2 (17.4 μA

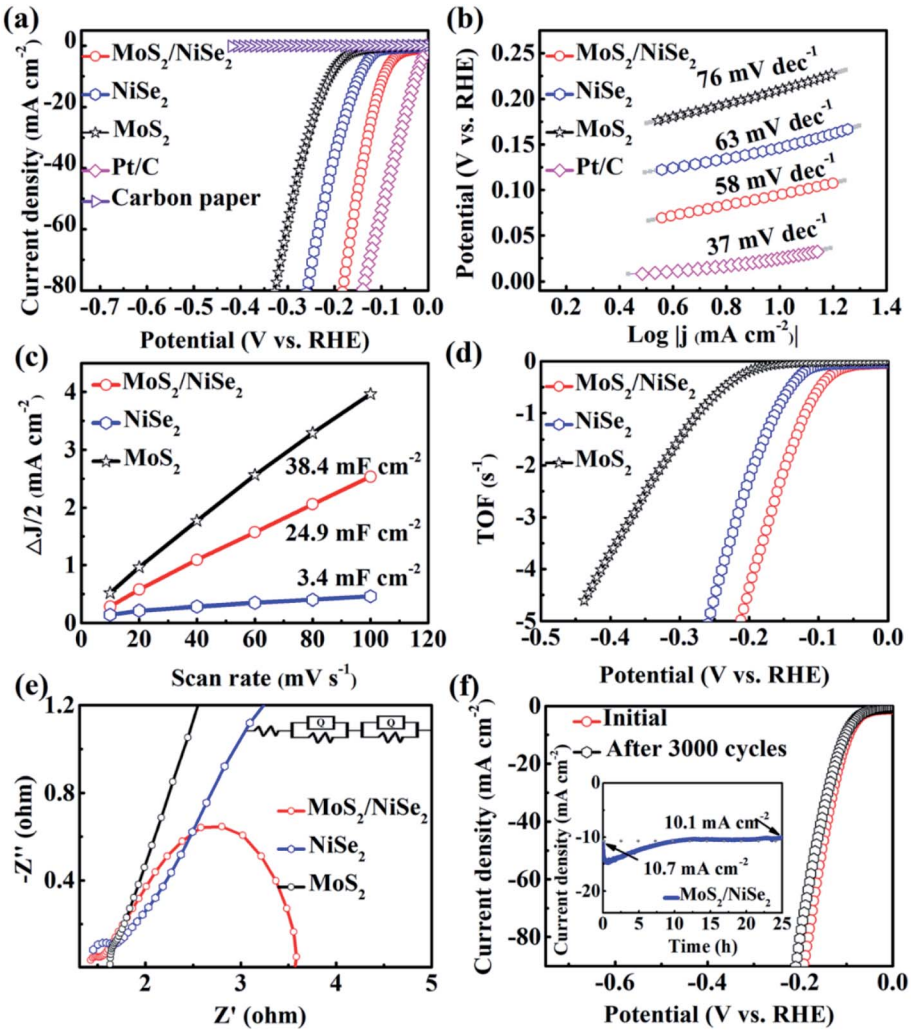

Fig. 4 (a) LSV data of MoS_2, $NiSe_2$, $MoS_2/NiSe_2$, Pt/C (20%) and carbon paper in 0.5 M H_2SO_4. (b) The relevant Tafel slopes. (c) Estimated values of double layer capacitance for MoS_2, $NiSe_2$, $MoS_2/NiSe_2$. (d) TOF data for HER of MoS_2, $NiSe_2$, $MoS_2/NiSe_2$. (e) Nyquist plots (100 mHz to 100 kHz) at −0.2 V (*vs.* RHE). The inset shows the corresponding equivalent circuit. (f) Polarization curves of $MoS_2/NiSe_2$ before and after cycling for 3000 times; inset shows chronoamperometric diagram of $MoS_2/NiSe_2$ at an overpotential of −100 mV (*vs.* RHE).

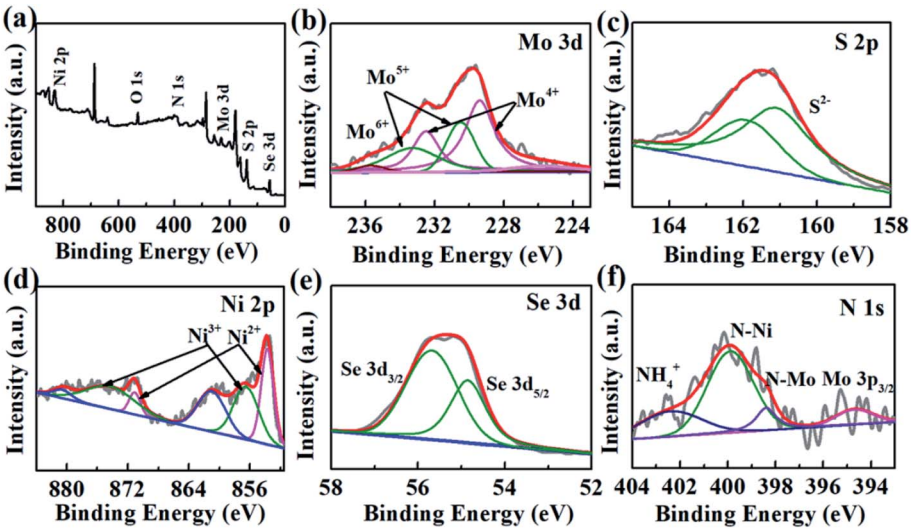

Fig. 5 (a) The survey, (b) Mo 3d, (c) S 2p, (d) Ni 2p, (e) Se 3d, (f) N 1s XPS spectra of MoS_2/$NiSe_2$ composite after cycling measurement.

cm^{-2}). In Fig. 4c, the C_{dl} value of 1T-MoS_2/N-doped $NiSe_2$ composite is derived from the CV curves in Fig. S6† and calculated to be 24.9 mF cm^{-2}. It is much larger than that of $NiSe_2$ (3.4 mF cm^{-2}) but slightly smaller than MoS_2 (38.4 mF cm^{-2}). Therefore, the enhanced HER activity of the composite must not mainly originate from high effective active area.[41] TOF is another important parameter for HER catalysts.[42] As shown in Fig. 4d and S7,† the composite needs 147 mV overpotential to reach a TOF value of 2 s^{-1}, while bare $NiSe_2$ and MoS_2 need an overpotential of 193 and 325 mV, respectively. It suggests that the inherent activity of bare $NiSe_2$ and MoS_2 have been dramatically enhanced by forming hybridized composite. This phenomenon can be related to the emergence of the large amount of interfaces between $NiSe_2$ and MoS_2.[43] The nonnegligible electronic coupling generated at these heterogeneous interfaces would result in the enhanced H-chemisorption and thus highly optimize the electrocatalytic activity in the HER. The EIS tests were conducted to analyze the intrinsic conductivity and kinetics of the catalysts. Fig. 4e shows the Nyquist plots of these catalysts at −0.2 V. The high-frequency intersection with the *x*-axis on the Nyquist plot represents the ohmic resistance (R_s), which expresses the overall interfacial contacts and the resistance of the electrolyte. The smallest R_s of the three catalysts indicates the strong interfacial contacts of 1T-MoS_2/N-doped $NiSe_2$ composite. The high-frequency half-arc is associated with the charge transfer resistance (R_{ct}). According to the equivalent circuit (inset in Fig. 4e), the 1T-MoS_2/N-doped $NiSe_2$ composite expresses a smaller R_{ct} of 0.25 Ω than bare $NiSe_2$ (0.37 Ω) and MoS_2 (0.55 Ω). The low-frequency semicircle represents the mass transfer resistance (R_{mt}). The mass transfer ability of 1T-MoS_2/N-doped $NiSe_2$ composite is also superior to the other two catalysts. These improvements after hybridizing should be attributed to the nonnegligible electronic couplings between $NiSe_2$ and MoS_2, the superior conductivity of $NiSe_2$ and the homogeneous distribution and further enlarged (002) interlayer spacing of 1T-MoS_2.

The durability of 1T-MoS_2/N-doped $NiSe_2$ composite was evaluated by 3000 times CV sweeping at 50 mV s^{-1}. In Fig. 4f, the polarization curve just exhibits an inappreciable decline after cycling. From another point of view, when 100 mV overpotential was applied, the current density decreases only 0.6 mA cm^{-2} after a chronoamperometric process for 25 hours (Inset of Fig. 4f). In Fig. S8,† the cycled 1T-MoS_2/N-doped $NiSe_2$ composite shows a similar morphology with the fresh composite in Fig. 2a. The structural information was also characterized by XRD test (Fig. S9†). The (002) peak of 1T-MoS_2 is still located at 8.7°, strongly confirming the robust microstructural stability of our 1T-MoS_2 as well as the 1T-MoS_2/N-doped $NiSe_2$ composite. The cycled composite was further analyzed by XPS. Fig. 5a manifests that all the elements of Mo, S, Ni, Se and N are maintained. In Fig. 5b–f, the same compositions and chemical surface states are shown as the profiles in Fig. 3. Especially, the proportion of NH_4^+ in the N 1s XPS spectrum is kept well after cycling (Fig. 5f), powerfully solidifying the structural stability of the 1T-MoS_2 synthesized in this study once again. Based on above analysis, it is reasonable to conclude that the 1T-MoS_2/N-doped $NiSe_2$ composite can afford the catalytic process for a long time, and its morphology, microstructure, and compositions can be kept well after the durability test.

4. Conclusions

In summary, 1T-MoS_2/N-doped $NiSe_2$ composite has been successfully fabricated *via* a solvothermal method. The composite achieves a 94 mV overpotential at 10 mA cm^{-2}, a small Tafel slope of 58 mV dec^{-1} and a good cycling durability in an acidic situation. Such promising HER performances should be attributed to: (i) the abundant exposed active edge sites arose from the ultrasmall size as well as the highly dispersed geometry of 1T-MoS_2 nanosheets; (ii) the intercalation of ammonium ions and further widened interplanar distance of 1T-MoS_2, which make electrolyte infiltrate into the catalyst more easily and sufficiently; (iii) the cocatalytic support of $NiSe_2$, which not only provides a conductive support to the

1T-MoS_2 nanosheets, but also serves as a cocatalyst for HER; (iv) the abundant interfaces with nonnegligible electronic coupling/interactions between MoS_2 and $NiSe_2$, which could facilitate the optimization of their electronic structure and then improve hydrogen adsorption. Given the above, this study offers a new option to realize stable 1T-MoS_2 and design efficient and low cost HER catalysts.

Conflicts of interest

The authors declare no competing financial interest.

Acknowledgements

This work was partially supported by the National Natural Science Foundation of China (No. 11504097, 51772069), and the Fundamental Research Funds for the Provincial Universities of Heilongjiang (Wu Li Li).

References

1 Q. Liu, Z. Xue, B. Jia, Q. Liu, K. Liu, Y. Lin, M. Liu, Y. Li and G. Li, *Small*, 2020, **16**, 2002482.
2 M. He, F. Kong, G. Yin, Z. Lv, X. Sun, H. Shi and B. Gao, *RSC Adv.*, 2018, **8**, 14369–14376.
3 H. Wang, X. Xiao, S. Liu, C. L. Chiang, X. Kuai, C. K. Peng, Y. C. Lin, X. Meng, J. Zhao, J. Choi, Y. G. Lin, J. M. Lee and L. Gao, *J. Am. Chem. Soc.*, 2019, **141**, 18578–18584.
4 J. Huang, D. Hou, Y. Zhou, W. Zhou, G. Li, Z. Tang, L. Li and S. Chen, *J. Mater. Chem. A*, 2015, **3**, 22886–22891.
5 K. Reilly, B. Fang, F. Taghipour and D. P. Wilkinson, *ACS Appl. Energy Mater.*, 2020, **3**, 8317–8329.
6 G. Liao, J. Fang, Q. Li, S. Li, Z. Xu and B. Fang, *Nanoscale*, 2019, **11**, 7062–7096.
7 G. Liao, Y. Gong, L. Zhang, H. Gao, G. J. Yang and B. Fang, *Energy Environ. Sci.*, 2019, **12**, 2080–2147.
8 J. Zhang, T. Wang, D. Pohl, B. Rellinghaus, R. Dong, S. Liu, X. Zhuang and X. Feng, *Angew. Chem.*, 2016, **128**, 6814–6819.
9 Y. Li, H. Wang, L. Xie, Y. Liang, G. Hong and H. Dai, *J. Am. Chem. Soc.*, 2011, **133**, 7296–7299.
10 J. Greeley, T. F. Jaramillo, J. Bonde, I. Chorkendorff and J. K. Norskov, *Nat. Mater.*, 2006, **5**, 909–913.
11 Y. Guo, T. Park, J. W. Yi, J. Henzie, J. Kim, Z. Wang, B. Jiang, Y. Bando, Y. Sugahara, J. Tang and Y. Yamauchi, *Adv. Mater.*, 2019, **31**, 1807134.
12 J. E. Lee, J. Jung, T. Y. Ko, S. Kim, S. I. Kim, J. Nah, S. Ryu, K. T. Nam and M. H. Lee, *RSC Adv.*, 2017, **7**, 5480–5487.
13 J. Xie, H. Zhang, S. Li, R. Wang, X. Sun, M. Zhou, J. Zhou, X. W. Lou and Y. Xie, *Adv. Mater.*, 2013, **40**, 5807–5813.
14 D. Wang, D. Zhang, C. Tang, P. Zhou, Z. Wu and B. Fang, *Catal. Sci. Technol.*, 2016, **6**, 1952–1956.
15 D. Wang, Y. Xiao, X. Luo, Z. Wu, Y. J. Wang and B. Fang, *ACS Sustainable Chem. Eng.*, 2017, **5**, 2509–2515.
16 M. A. Lukowski, A. S. Daniel, F. Meng, A. Forticaux, L. Li and S. Jin, *J. Am. Chem. Soc.*, 2013, **135**, 10274–10277.
17 Z. He and W. Que, *Appl. Mater. Today*, 2016, **3**, 23–56.
18 Z. Wu, C. Tang, P. Zhou, Z. Liu, Y. Xu, D. Wang and B. Fang, *J. Mater. Chem. A*, 2015, **3**, 13050–13056.
19 G. Suo, D. Li, L. Feng, X. Hou, X. Ye, L. Zhang, Q. Yu, Y. Yang and W. Wang, *J. Mater. Sci. Technol.*, 2020, **55**, 167–172.
20 D. Li, J. Zhang, S. M. Ahmed, G. Suo, W. Wang, L. Feng, X. Hou, Y. Yang, X. Ye and L. Zhang, *J. Colloid Interface Sci.*, 2020, **8**, 174–181.
21 G. Suo, J. Zhang, D. Li, Q. Yu, M. He, L. Feng, X. Hou, Y. Yang, X. Ye, L. Zhang and W. Wang, *J. Colloid Interface Sci.*, 2020, **566**, 427–433.
22 G. Suo, J. Zhang, D. Li, Q. Yu, W. Wang, M. He, L. Feng, X. Hou, Y. Yang, X. Ye and L. Zhang, *Chem. Eng. J.*, 2020, **388**, 124396.
23 Q. Liu, Q. Fang, W. Chu, Y. Wan, X. Li, W. Xu, M. Habib, S. Tao, Y. Zhou, D. Liu, T. Xiang, A. Khalil, X. Wu, M. Chhowalla, P. M. Ajayan and L. Song, *Chem. Mater.*, 2017, **29**, 4738–4744.
24 M. R. Gao, J. X. Liang, Y. R. Zheng, Y. F. Xu, J. Jiang, Q. Gao, J. Li and S. H. Yu, *Nat. Commun.*, 2015, **6**, 5982.
25 J. Lin, P. Wang, H. Wang, C. Li, X. Si, J. Qi, J. Cao, Z. Zhong, W. Fei and J. Feng, *Adv. Sci.*, 2019, **6**, 1900246.
26 X. Chen, Z. Wang, Y. Wei, X. Zhang, Q. Zhang, L. Gu, L. Zhang, N. Yang and R. Yu, *Angew. Chem., Int. Ed.*, 2019, **58**, 17621–17624.
27 B. Yu, X. Wang, F. Qi, B. Zheng, J. He, J. Lin, W. Zhang, Y. Li and Y. Chen, *ACS Appl. Mater. Interfaces*, 2017, **9**, 7154–7159.
28 Q. Liu, X. Li, Q. He, A. Khalil, D. Liu, T. Xiang, X. Wu and L. Song, *Small*, 2015, **11**, 5556–5564.
29 Y. J. Tang, Y. Wang, X. L. Wang, S. L. Li, W. Huang, L. Z. Dong, C. H. Liu, Y. F. Li and Y. Q. Lan, *Adv. Energy Mater.*, 2016, **6**, 1600116.
30 R. Zhang, W. Wan, D. Li, F. Dong and Y. Zhou, *Chin. J. Catal.*, 2017, **38**, 313–320.
31 A. Long, W. Li, M. Zhou, W. Gao, B. Liu, J. Wei, X. Zhang, H. Liu, Y. Liu and X. Zeng, *J. Mater. Chem. A*, 2019, **7**, 21514–21522.
32 G. M. Bremmer, L. V. Haandel, E. J. M. Hensen, J. W. M. Frenken and P. J. Kooyman, *Appl. Catal., B*, 2019, **243**, 145–150.
33 B. Tang, Z. G. Yu, Y. Zhang, C. Tang, H. L. Seng, Z. W. Seh, Y. W. Zhang, S. J. Pennycook, H. Gong and W. Yang, *J. Mater. Chem. A*, 2019, **7**, 13339–13346.
34 T. Kou, T. Smart, B. Yao, I. Chen, D. Thota, Y. Ping and Y. Li, *Adv. Energy Mater.*, 2018, **8**, 1703538.
35 W. Li, B. Yu, Y. Hu, X. Wang, D. Yang and Y. Chen, *ACS Sustainable Chem. Eng.*, 2019, **7**, 4351–4359.
36 J. Zhu, Z. C. Wang, H. Dai, Q. Wang, R. Yang, H. Yu, M. Liao, J. Zhang, W. Chen, Z. Wei, N. Li, L. Du, D. Shi, W. Wang, L. Zhang, Y. Jiang and G. Zhang, *Nat. Commun.*, 2019, **10**, 1348.
37 J. Chen, X. J. Wu, Y. Gong, Y. Zhu, Z. Yang, B. Li, Q. Lu, Y. Yu, S. Han, Z. Zhang, Y. Zong, Y. Han, L. Gu and H. Zhang, *J. Am. Chem. Soc.*, 2017, **139**, 8653–8660.
38 C. Liu, T. Gong, J. Zhang, X. Zheng, J. Mao, H. Liu, Y. Li and Q. Hao, *Appl. Catal., B*, 2020, **262**, 118245.

39 S. Han, Y. Hao, Z. Guo, D. Yu, H. Huang, F. Hu, L. Li, H. Y. Chen and S. Peng, *Chem. Eng. J.*, 2020, **401**, 126088.
40 Y. Yi, Z. Sun, C. Li, Z. Tian, C. Lu, Y. Shao, J. Li, J. Sun and Z. Liu, *Adv. Funct. Mater.*, 2020, **30**, 1903878.
41 B. Zhang, J. Liu, J. Wang, Y. Ruan, X. Ji, K. Xu, C. Chen, H. Wan, L. Miao and J. Jiang, *Nano Energy*, 2017, **37**, 74–80.
42 J. Kibsgaard and T. F. Jaramillo, *Angew. Chem., Int. Ed.*, 2014, **53**, 14433–14437.
43 C. Tsai, F. A. Pedersen and J. K. Nørskov, *Nano Lett.*, 2014, **14**, 1381–1387.